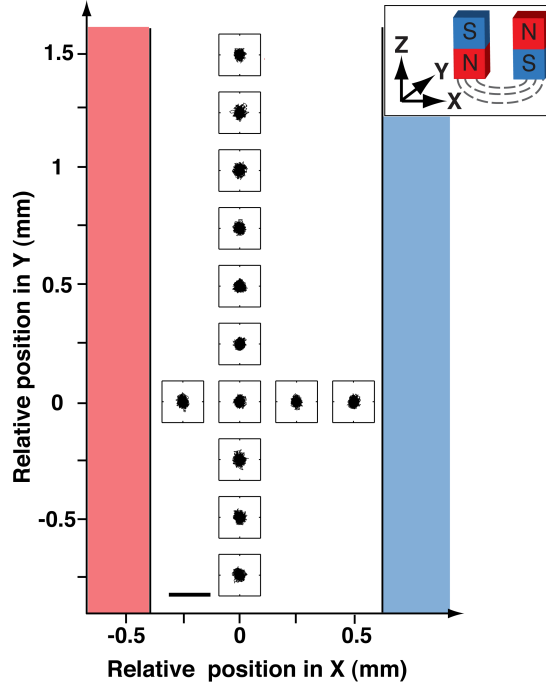**Supplementary Figure S1.** Schematics of conventional magnetic tweezers and freely-orbiting magnetic tweezers. (a) Schematic of conventional magnetic tweezers. A superparamagnetic bead is tethered to a flow cell surface via a dsDNA construct with multiple attachment points at both ends. A pair of permanent magnets exerts a magnetic field that is aligned horizontally. The preferred magnetization axis m_0 of the superparamagnetic bead aligns with the horizontal magnet field and the rotation of the bead about the z-axis is tightly constrained. A reference bead is attached to the flow cell surface and tracked simultaneously to correct for mechanical drift. (b) Schematic of freely-orbiting magnetic tweezers. The superparamagnetic bead, reference bead, and DNA tether are identical to the conventional magnetic tweezers. In contrast to conventional magnetic tweezers, a cylindrical magnet is employed with the field predominantly aligned in the z-direction. For this magnet geometry, the preferred magnetization axis m_0 aligns with the vertical magnetic field and the bead can freely rotate about the z-axis.
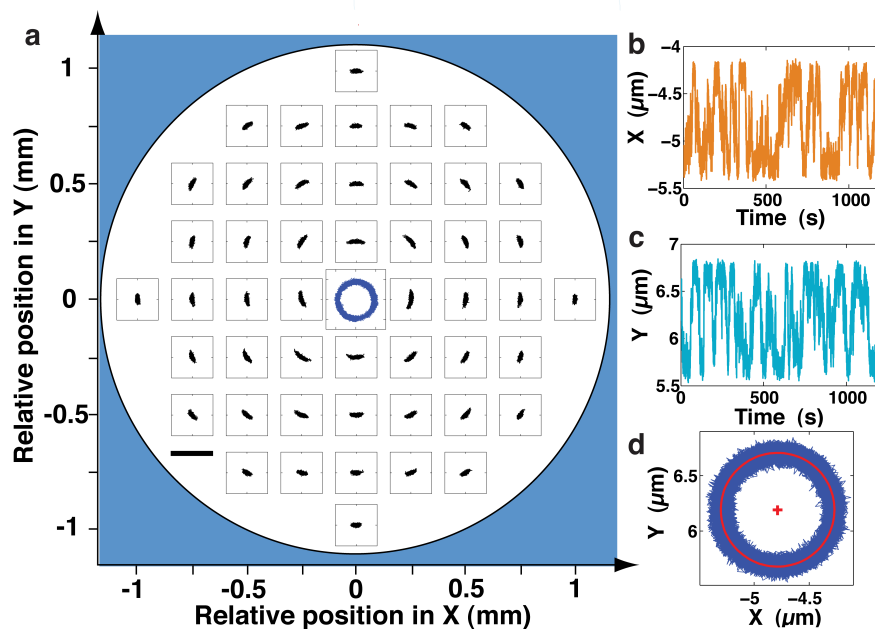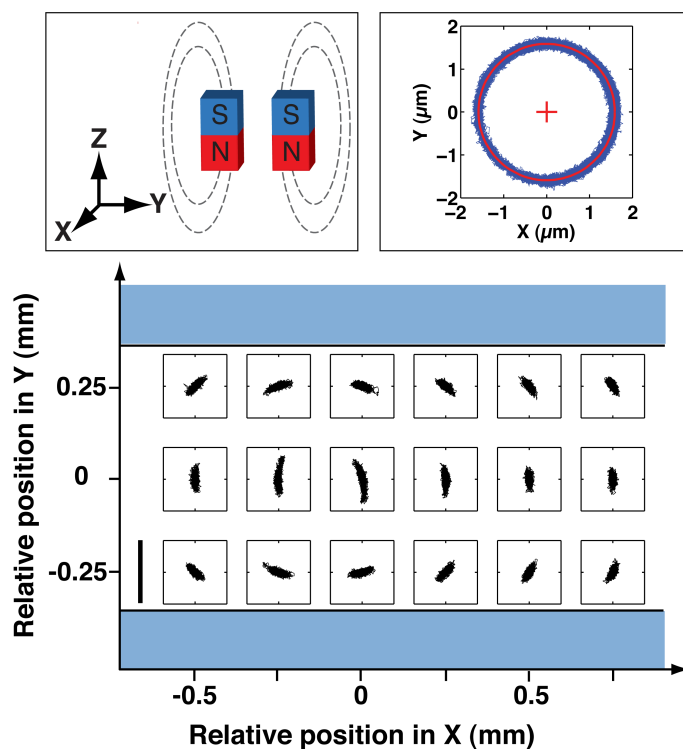
Supplementary Figure S2. Fluctuations in (x,y) of a bead tethered to a 7.9 kbp DNA under a cylindrical magnet as a function of magnet position. (a) (x, y)-fluctuations of the bead's center position as a function of the position of the bead relative to the cylindrical magnet. The position of the cylindrical magnet (shown schematically in Supplementary Figure S1b) was scanned at a constant height of 3 mm across the flow cell surface in fixed steps of 250 μm in x and y. The position of the bead relative to the magnet is indicated on the outer plot axes. Our scan range is limited by the 2 mm central opening of the magnet, since we illuminate the flow cell from the top through the central aperture of the magnet. Inaccessible positions are indicated by the blue shading in the plot. At each magnet position, fluctuations of the same DNA-tethered bead were recorded, which are plotted in the small square coordinate systems. The scale of the fluctuations is indicated by the black scale bar which corresponds to 2 μm. A systematic variation of the (x, y) fluctuation pattern with magnet position resembling a cyclone or vortex is apparent. In the case of a perfectly centered alignment of the magnet, the bead's (x, y)-fluctuations trace out a circular trajectory, plotted in blue in the center of the plot. The blue trace was recorded in a separate experiment after aligning the magnets in smaller steps about the center and is shown for illustration in this plot. (b-d) Example traces of the x and y fluctuations of a DNA-tethered bead under a well-aligned cylindrical magnet. The traces of x (b) and y (c) as a function of time reveal slow and correlated fluctuations. (d) Plot of the same data as in (b) and (c), shown as x vs. y with a fitted circle and fitted center position (red line and red cross).
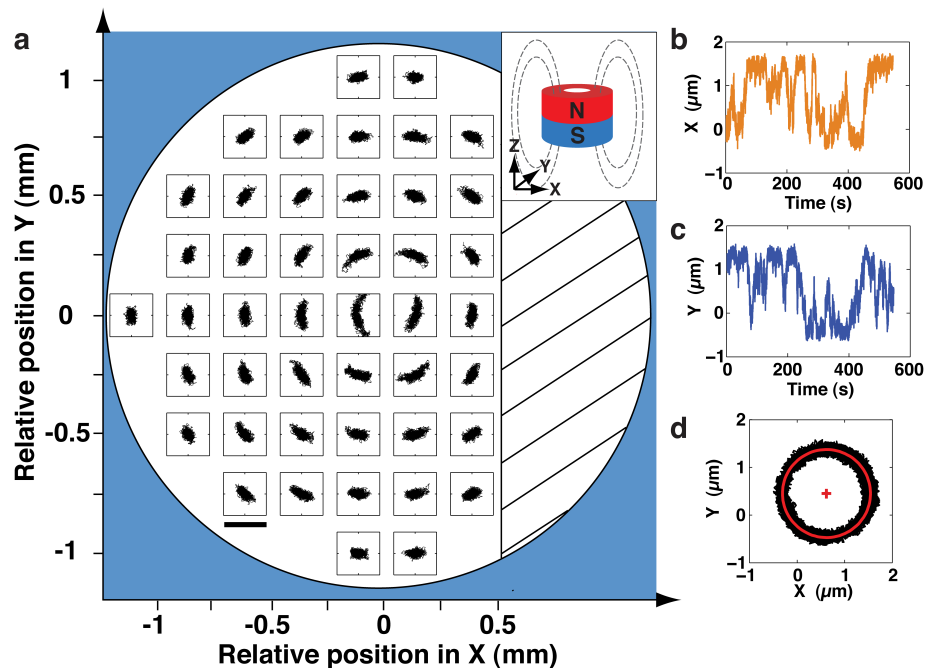
Supplementary Figure S3. The (x, y)-fluctuations of a superparamagnetic bead tethered by a 20.6 kbp DNA construct under a cylindrical magnet as a function of magnet position. (a) (x, y)-fluctuations as a function of the position of the bead relative to the cylindrical magnet (shown schematically in the inset). The cylindrical magnet was scanned across the flow cell surface at a constant height of 3 mm in fixed steps of 250 μm in x and y. The bead positions relative to the magnet are indicated on the outer axes. The central hole of the magnet has a diameter of 2 mm, limiting the scan range to a circle of 2 mm diameter, indicated schematically by the blue shading in the plot. For this measurement, the scan range was additionally limited by the range of the stage displacing the magnet in x, indicated by the hatched area. At each magnet position, fluctuations of the same DNA tethered bead were recorded and are plotted in the small square coordinate systems throughout the plot. The scale of the fluctuations is indicated by the black scale bar which corresponds to 2 μm. Systematic variations of the (x, y)-fluctuation patterns, very similar to Supplementary Fig. S2a, are apparent. (b-d) Example trace of the x and y fluctuations of a bead tethered by a 20.6 kbp DNA construct under a well-aligned cylindrical magnet. The traces of x (b) and y (c) as a function of time reveal slow and correlated fluctuations. (d) Plot of the (x, y) trajectory of the same data as in b and c, with a fitted circle (red line) and fitted center position (red cross).
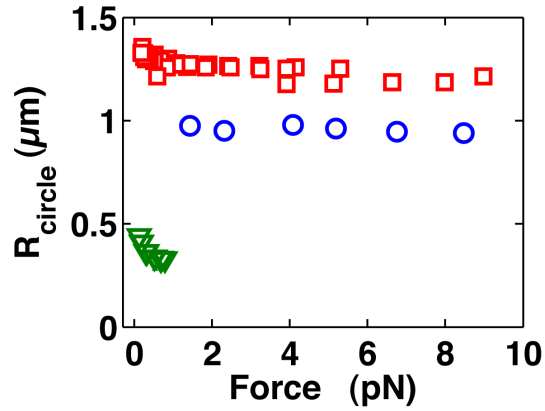
Supplementary Figure S4. The (x, y)-fluctuations of a DNA-tethered bead as a function of magnet position in conventional magnetic tweezers. The experiment used two 5 mm cube magnets with a gap of 1 mm, shown schematically in the inset in the upper right corner. The magnet was scanned across the surface at a constant height of 2 mm in x and y in steps of 250 μm. The bead positions relative to the magnets are indicated on the outer axes. Similar to the measurements with the cylindrical magnets, we illuminate from the top through the central magnet gap, limiting the scan range in the x dimension to 1 mm. The graph shows a limited scan in the y-direction around the center of the pair of 5 mm wide magnets. At each magnet position, fluctuations of the same DNA tethered bead were recorded, which are plotted in the small square coordinate systems throughout the plot. The scale of the fluctuations is indicated by the black scale bar which corresponds to 2 μm. From the plot it is apparent that the fluctuations in x and y are insensitive to the magnet position. The width of the fluctuations in y is consistently somewhat larger than the width of the fluctuations in x, stemming from the fact that the preferred magnetic axis of the bead, m_0, is tightly constrained to remain parallel the field lines, which point in the direction of the x-axis. This prevents the bead from rotating about the y-axis in as it translates in the x-direction and fluctuations in this dimension are governed by an effective tether length equal to L, the length of the DNA tether. In contrast, the bead can freely rotate about the x-axis as it translates in the y-direction, and the fluctuations in this dimension are governed by an effective tether length of $L + R_{\mathrm{bead}}$, reducing the effective spring constant (see Ref. 9 in the main text).

Supplementary Figure S5. The (x, y)-fluctuations of a DNA-tethered bead as a function of magnet position for a pair of vertical-parallel magnets. The position of the pair of magnets (shown schematically in the upper left inset) was scanned at a constant height of 3 mm across the flow cell surface in fixed steps of 250 μm in x and y. The bead position relative to the magnets are indicated on the outer axes. We employed a magnet geometry with a central gap of 0.5 mm, limiting the scan range in the y dimension to 0.5 mm. The extent of the magnets in x is 5 mm, the graph shows a limited scan in x around the central region of the magnets. At each magnet position, fluctuations of the same DNA tethered bead were recorded and are plotted in the small square coordinate systems throughout the plot. The scale of the fluctuations is indicated by the black scale bar which corresponds to 2 μm. Similar to the case of cylindrical magnet scan (Supplementary Fig. S2 and S3) a systematic variation of the (x, y)-fluctuation pattern with magnet position resembling a cyclone or vortex is apparent. In the case of a perfectly centered alignment of the pair of magnets with the bead, the bead's (x, y)-fluctuations trace out a circular trajectory, plotted in blue in the upper right inset. The blue data trace was recorded in a separate experiment after carefully aligning the magnets to the center of the cyclone pattern; the fitted circle is shown as a red line.
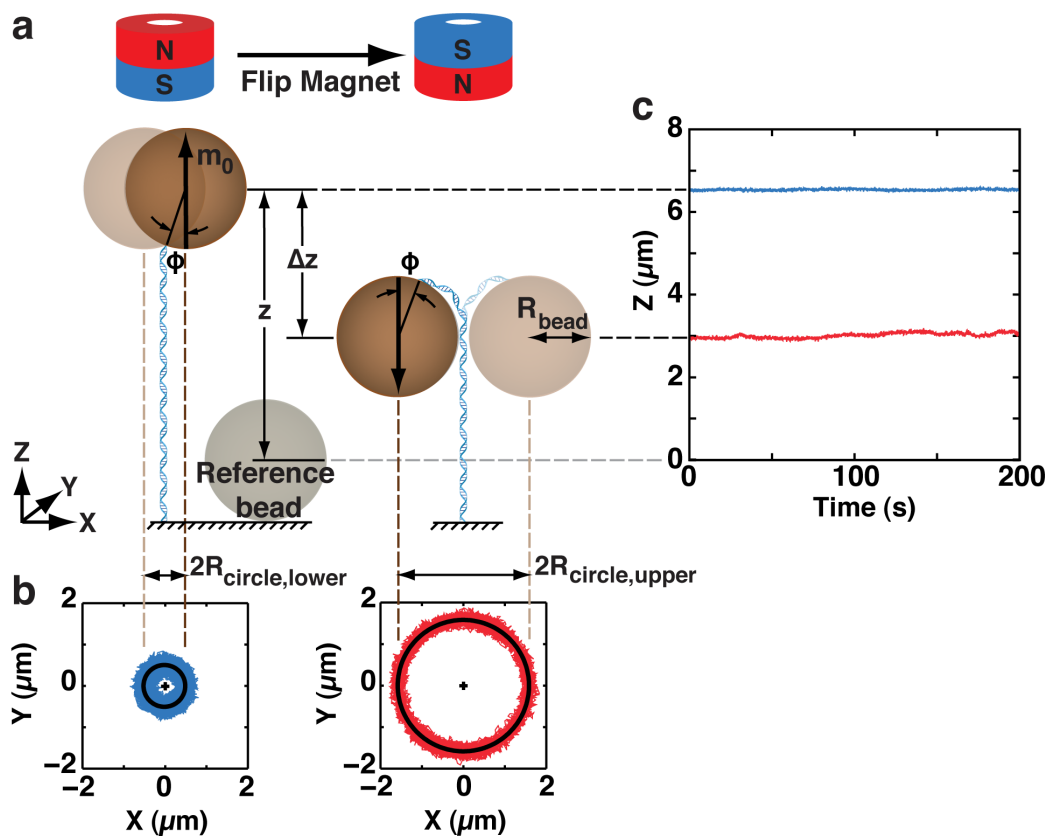
Supplementary Figure S6. Dependence of the (x, y, z)-trajectories on the magnetic field orientation under the cylindrical magnet. Trajectories are shown for the same 1.4 μm radius superparamagentic M270 bead tethered by a 20.6 kbp DNA at $\approx$ 2.5 pN applied force. (a) Schematic of the measurement. Trajectories are recorded in both magnet orientations (i.e. north up and north down) after aligning the magnet over the bead in each case. The large arrow on the bead indicates the orientation of the preferred magnetic axis m_0. (b) (x, y)-trajectories for typical measurement in both magnet orientations: north up (blue, left panel) and north down (red, right panel). Fits to a circle are shown in black, with the fitted center shown as a black cross. Flipping the magnet changes the radius from 0.50 μm to 1.58 μm. (c) The measured height $\langle z \rangle$ of the bead above the flow cell surface for the magnet in both orientations. Trace colors correspond to panel (b). Flipping the magnet decreases the bead height above the surface from 6.54 μm (north up) to 3.02 μm (north down). Results from similar measurements are shown in Supplementary Table S1, and demonstrate that while changes in both the bead height and the circle radius vary from bead to bead, large changes in R_{circle} upon magnet flipping correlate with large changes in $\langle z \rangle$.

Supplementary Figure S7. Dependence of R_{circle} on the stretching force. We determined the values for R_{circle} from fits to the (x, y)-fluctuations and the stretching forces as described in the main text. Data correspond to selected measurements for 7.9 kbp DNA tethers and 1.4 μm radius M270 beads (red squares), for 20.6 kbp DNA tethers and M270 beads (blue circles), and for 3.4 kbp DNA and ≈ 0.3 μm radius MagSense beads (green triangles). Overall the observed R_{circle} does not depend on stretching force. At low stretching forces (≤ 0.5 pN), we observe small increases in R_{circle}, by 10-20%. This is qualitatively expected from the geometry of the tether: At forces ≤ 0.5 pN, entropic recoil of the DNA would be expected to lead to excluded volume interactions with the bead, biasing radial fluctuations towards larger radii. Experimentally, we indeed observe that the radial fluctuations for very low stretching forces show small deviations from Gaussian behavior with a bias towards larger radii (data not shown).
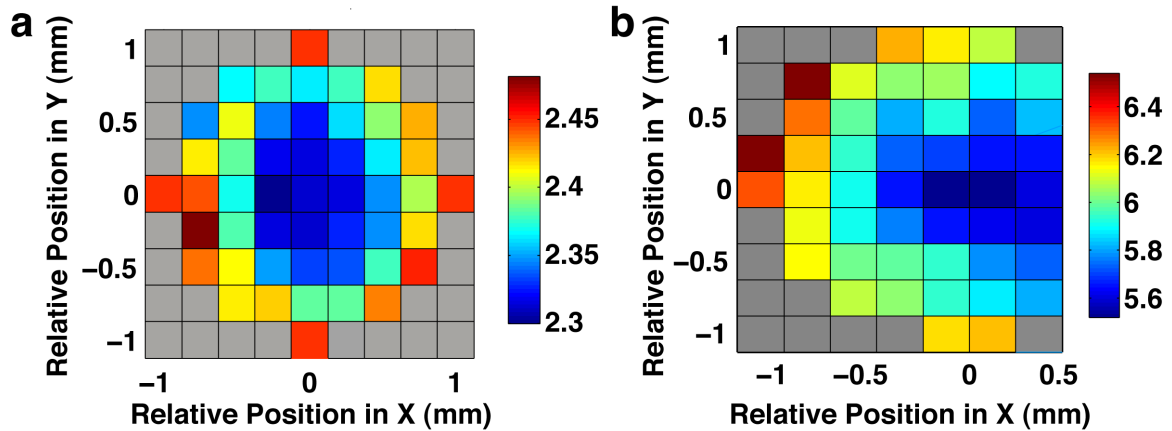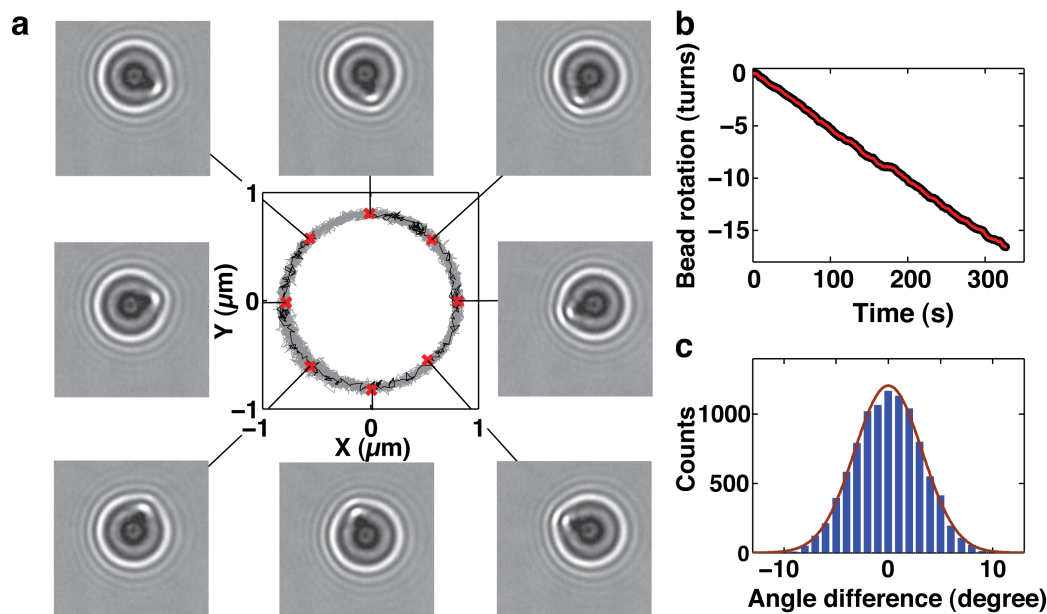
Supplementary Figure S8. Height of tethered beads above the surface, $\langle z \rangle$, as a function of alignment of the cylindrical magnet. Color indicates $\langle z \rangle$, according to scale bars on each plot. (a) Data for a 7.9 kbp DNA tether and 1.4 μm radius bead. This is the bead height information corresponding to the data set shown in Supplementary Fig. S2a. (b) Data for a 20.6 kbp DNA tether and 1.4 μm radius bead. This is the bead height information corresponding to the data set shown in Supplementary Fig. S3a. For this measurement, the scan range was limited by the range of the stage displacing the magnet in x (see also Supplementary Fig. S3). For this reason, the pattern is not symmetric.

For both panels, the average height of the bead above the surface increases as the bead moves away from the magnet center. This can be understood qualitatively from simple geometric considerations (Supplementary Fig. S1a,b). If the tether is attached such that $R_{\text{circle}} > R_{\text{bead}}/\sqrt{2}$ (i.e. a tether anchored at an angle of $> \pi/4$ radians with respect to vertical), the height of the bead above the surface $\langle z \rangle$ will be smallest close to the magnet center where we observe circular fluctuations. Far from center alignment, the bead will rise as m_0 rotates to align with the more horizontal field lines, similar to the situation in conventional magnetic tweezers.
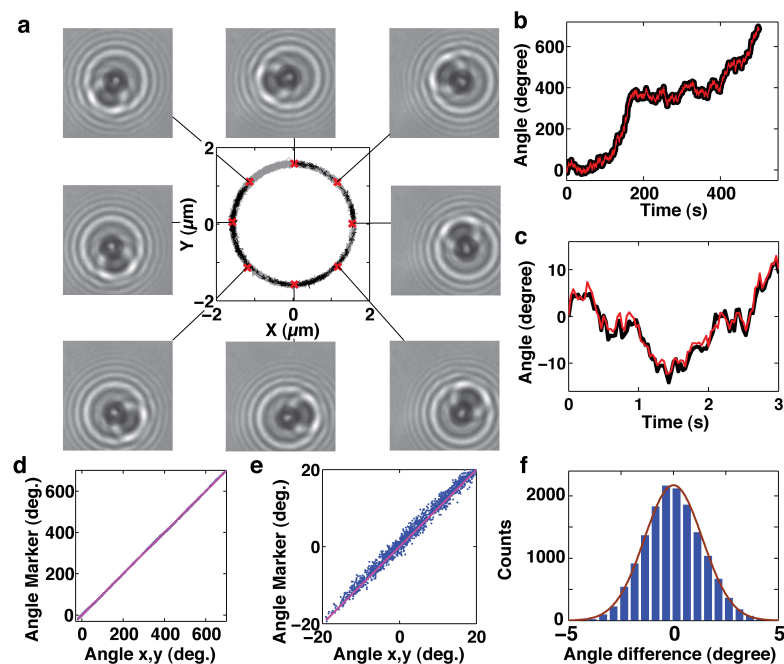
Supplementary Figure S9. Comparison of the rotation angle determined from direct tracking of a fiducial marker bead and from the bead's position in the (x, y)-plane. The measurement demonstrates that bead rotation and bead translation on the circular annulus are tightly coupled. (a) The central panel shows the x, y-fluctuations of a tethered 1.4 μm radius magnetic bead under the centrally aligned cylindrical magnet. A 0.5 μm radius non-magnetic bead is attached to the tethered magnetic bead and acts as a fiducial marker to detect rotation. All (x, y)-positions are shown in grey. For selected frames (indicated by red crosses) from a subsection of the trajectory (shown as the black trace) the corresponding CCD camera images are shown. The bead images are ~ 4 μm out of focus to facilitate x, y, and z tracking of the bead's position. From the images it is apparent that there is a fixed relationship between the rotation of the bead (traceable from the relative position of the small marker bead) and the position of the bead on the circular annulus in the x, y-plane. The position of the fiducial marker rotates in synchrony with the beads position on the circular annulus, maintaining an angle of $\sim 5°$ counterclockwise from the tangent vector. (b) Rotation angle of the bead determined from the position of the fiducial marker bead (red) and from the position in the (x, y)-plane (black). The tracking algorithms are described in the "Methods" section. (c) Zoom of the trace in (b), focusing on the first three seconds. The red and black trace are clearly distinct, but track each other closely. (d) Plot of the bead's rotation angle determined from the direct tracking of the fiducial marker bead vs. the angle determined from the position in the (x, y)-plane (blue points). A line with a slope of one is shown in magenta. The correlation coefficient between the two angle data sets is $r = 0.999973$. (e) Zoom of the correlation plot in (d), focusing on the region from -20 to +20 degrees. (f) Histogram of the difference in angle determined from the position of the fiducial bead and the angle determined from the position in the (x, y)-plane (over the full trace shown in panel a). The brown line is a Gaussian fit with $\sigma = 1.38°$. The data were obtained using the 7.9 kbp DNA construct in PBS+ buffer.

Supplementary Figure S10. Bead rotation and bead translation on the circle are tightly coupled for a rotating bead. (a) The central panel shows the x, y-position under the centrally aligned cylindrical magnet of a tethered 1.4 μm radius magnetic bead that has a 0.5 μm radius non-magnetic bead attached. In contrast to the data shown in Supplementary Fig. S9, the trace here was recorded after flushing a high concentration of ethidium bromide into the flow cell. Ethidium is known to intercalate into double-stranded DNA and to unwind the DNA helix [38]. All (x, y)-positions are shown in grey in the central panel. For selected frames (indicated by red crosses) from a subsection of the trajectory (shown as the black trace) the corresponding bead images are shown. The bead images are ~3 μm out of focus to facilitate x, y, and z tracking of the bead's position. From the images it is apparent that there is a fixed relationship between the rotation of the bead (traceable from the relative position of the small marker bead) and the position of the bead on the circle in the (x, y)-plane. (b) Rotation angle of the bead determined from the position of the fiducial marker bead (red; see "Methods") and from the position in the x, y-plane (black). While still undergoing Brownian fluctuations, the bead systematically rotates, by $\approx$ -16 turns in the trace presented, due to ethidium intercalation unwinding the DNA helix. The correlation coefficient between the two angle data sets is $r = 0.9999983$. (c) Histogram of the difference in angle determined from the position of the fiducial bead and the angle determined from the position in the (x, y)-plane. The brown line is a Gaussian fit with $\sigma = 3.24°$. The data were obtained using the 20.6 kbp DNA construct in PBS+ buffer.
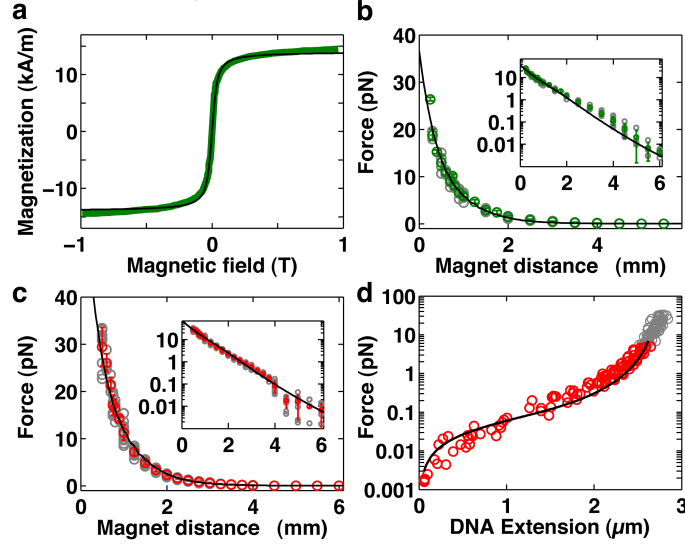
Supplementary Figure S11. Force predictions for a conventional MT magnet configuration and M280 and M270 superparamagnetic beads. The magnetization parameters determined from the measurements using the conventional MT magnet configurations are used to quantitatively predict the forces exerted by the cylinderical magnet (Fig. 2 and Supplementary Fig. S12). Since there is no literature value for the magnetization of M270 beads, we used the magnetization of the M280 beads as a starting point to analyze the M270 data, see below. (a) Magnetization of Dynalbeads M280 superparamagnetic beads as a function of the applied magnetic field. Experimental data (thick green line) determined by Fonnum *et al.* [39] and a fit of the Langevin function [40] (thin black line):

$$m(B) = m_{sat} \left(\coth(B/B_0) - \frac{1}{B/B_0} \right)$$

with the saturation magnetization $m_{sat} = 13.97$ kA/m and the characteristic field $B_0 = 15.5$ mT as fitting parameters. (b) Measured and predicted forces for M280 beads and a pair of magnets in the horizontal magnet configuration with a gap between the magnets of 1 mm and an iron yoke connecting the magnets. The force prediction (black line) is computed taking into account the magnetization from panel (a) and the magnetic field as described in Lipfert *et al.* (Ref. 8). Experimental data are obtained from three independent measurements; all data points are shown as grey circles. The mean and standard deviation of the force values for each magnet position are shown as green circles and error bars. The inset shows the same data as a logarithmic plot. We note that the black line is not a fit to the data, but a prediction from the independently determined magnetization and magnetic field. (c) Measured and predicted forces for M270 beads and a conventional MT magnet configuration (the same magnet configuration as panel b). Experimental data are obtained from seven independent measurements; all data points are shown as grey circles. The mean and standard deviation of the force values for each magnet position are shown as red circles and error bars. Since there is no literature value for the magnetization of M270 beads, we used the magnetization of the M280 beads (panel a) as a starting point to analyze the M270 data. For each magnet position, the measured forces are higher for M270 than for M280 beads; we obtained good agreement between calculated and measured forces for M270 beads by using the magnetization for M280 beads with m_{sat} scaled by a factor of 2 ± 0.1 (black line). The inset shows the same data as a logarithmic plot. (d) DNA stretching data for the 7.9 kbp DNA construct in PBS+ buffer with M270 beads (same data as panel c). The black line is a fit of the WLC chain model to the data in the entropic stretching regime (< 5 pN; red data points) with $L_p = 43 \pm 3$ and $L_c = 2.75 \pm 0.1$ μm.
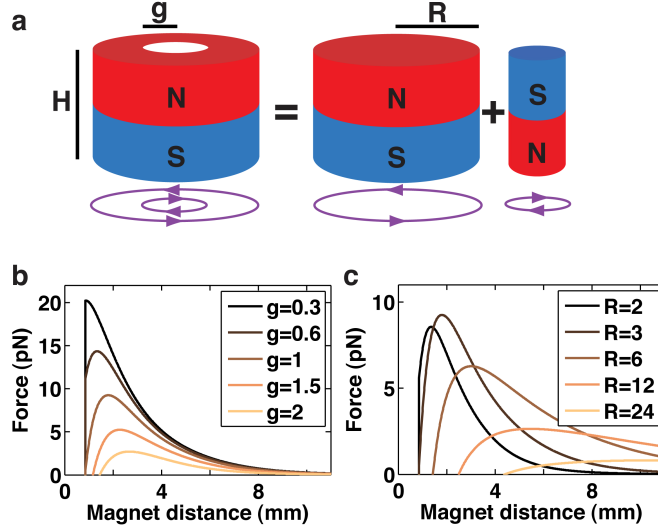
Supplementary Figure S12. Calculation of the magnetic field and stretching forces applied to superparamagnetic beads for cylindrical magnets. (a) The magnetic field from a permanent magnet can be calculated using the equivalent source method that relies on approximating the magnet by equivalent magnetizing currents. The cylindrical magnet with a central hole (left) used in our measurements is equivalent to the superposition of a solid cylindrical magnet of equal size and magnetization and a smaller solid cylindrical magnet that has the size of the central hole and opposite magnetization (right). The equivalent current loops are shown below the magnets. The dimensions of the magnet are defined by its radius R, the radius of the central hole g, and its height H. For the magnet used in our experiments $R = 3$ mm, $g = 1$ mm, and $H = 6$ mm. The magnet field can be calculated from Biot-Savart law by integrating over the equivalent current loop (Ref. 8 in the main text):

$$\vec{B} = \frac{\mu_0}{4\pi} \int J_{equi} \frac{d\hat{l} \times \hat{r}}{r^2} = \frac{B_r}{4\pi} \int \frac{d\hat{l} \times \hat{r}}{r^2}$$

where $\hat{l}$ is a unit vector pointing in the direction of the equivalent current and $\vec{r}$ is the coordinate vector from the element of current to the observation point. J_{equi} is the equivalent current that is given by $B_r/4\pi$, where B_r is the residual magnetic field of the magnet, which is a material property. We have determined B_r for the magnets used in our experiment as described in Lipfert *et al.* to be $B_r = 1.25$ T (Ref. 8 in the main text). The integral in the equation for $\vec{B}$ can be solved analytically for the cylindrical magnet geometry to compute the z component of the magnetic field along the z-axis (taken as the line of symmetry of the cylinder with the coordinate origin centered on the cylinder):

$$
\begin{aligned}
B_z(z) \quad = \quad & \frac{B_r}{2}\left(\left(\frac{z + H/2}{\sqrt{R^2 + (z + H/2)^2}} - \frac{z - H/2}{\sqrt{R^2 + (z - H/2)^2}}\right)\right.\\
& \left.-\left(\frac{z + H/2}{\sqrt{g^2 + (z + H/2)^2}} - \frac{z - H/2}{\sqrt{g^2 + (z - H/2)^2}}\right)\right)
\end{aligned}
$$

The ability to quantitatively predict forces for a choice of beads and magnet geometries can be used to optimize the configuration for particular experimental requirements. (b) Predictions of the forces exerted on M270 beads using the same magnet properties as above and systematically varying the gap size (see legend). (c) Predictions of the forces exerted on M270 beads using the same magnet properties as above and systematically varying the radius of the magnet (see legend).
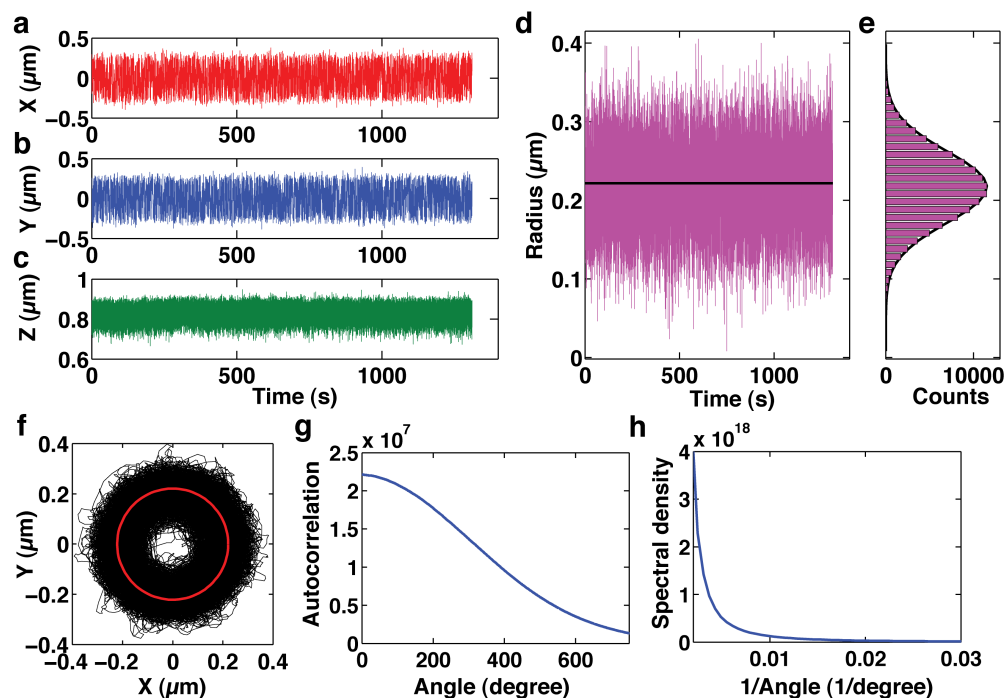
Supplementary Figure S13. Fluctuations of a 0.35 μm radius MagSense bead tethered by 3.4 kbp DNA construct in the FOMT. The data shown are the same trace that is analyzed in Fig. 3a-f. (a-c) The x, y, and z fluctuations of the bead. (d) Fluctuations of the radial coordinate, determined from the (x, y)-position. The solid black line is the fitted radius of the circle, see also panel (f). (e) Histogram of the radial fluctuations shown in panel d. The black line is a Gaussian fit with a width of $\sigma = 0.045$ μm. (f) The (x, y)-fluctuations of the bead (black) lie on a circle (red line). (g) Pairwise autocorrelation function of the rotational fluctuations. The correlation is essentially featureless, in particular, there are no discernible peaks at 360 or 720° that would correspond to full turns. (h) Fourier transform of the pairwise autocorrelation function of the rotational fluctuations. Similar to panel (j), no clear features are discernible, indicating that there are no preferred positions on the circle. The measurement was carried out in PBS+ buffer (Methods).
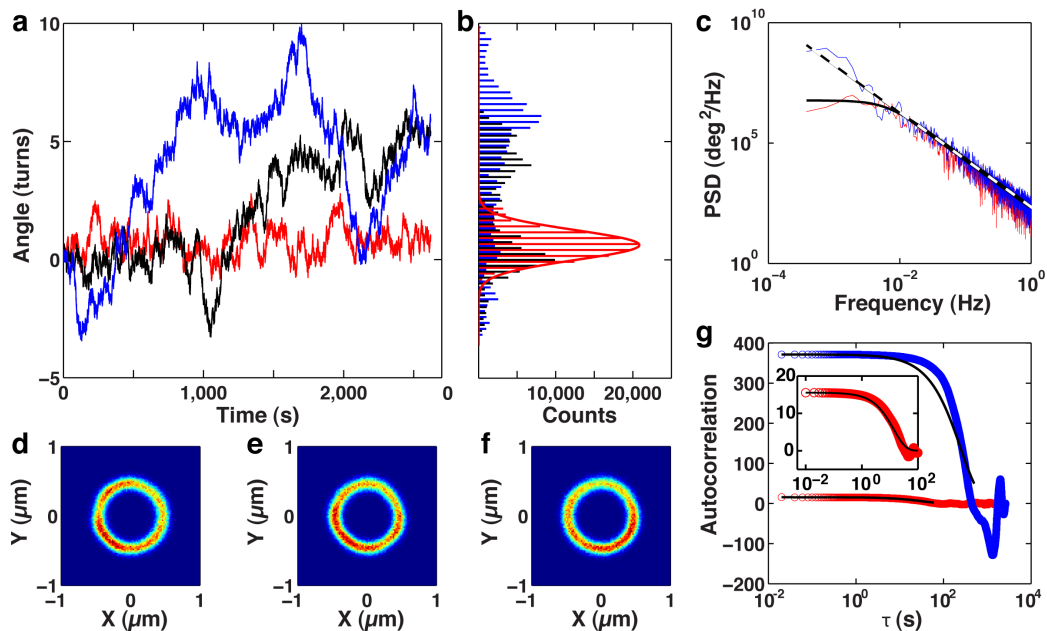
Supplementary Figure S14. The effects of DNA rotational constraint on the angular fluctuations. Data shown are for a MyOne bead tethered to 3.4 kbp DNA which lost its rotational constraint during the experiment. (a) Three angle vs. time traces recorded for the same bead. During the first trace (red) the bead is rotationally constrained. During the second trace (black) the bead loses its rotational constraint at about 1,000 s. During the third trace (blue), the bead is unconstrained, and explores a much wider range of angles than in the first trace. Colors in all subsequent plots correspond to those in a). (b) Histograms of angular position. While still rotationally constrained, the bead's rotational fluctuations are Gaussian-distributed. The Gaussian fit (red line) gives a standard deviation of 0.62 turns (226°). A similar, smaller peak is observed during the second trace; however, contributions following nicking lead to a much broader random distribution overall. The histogram for third trace is entirely stochastic. (c) Power spectra of the angular fluctuations for constrained (red) and unconstrained (blue) recordings. The power spectrum while the molecule is rotationally constrained is well-described by a Lorentzian (black solid line), as expected for diffusion within a harmonic trap. The fitted corner frequency is $f_c = 0.01$ Hz. After rotational constraint is lost, the power spectrum follows a power law, PSD $\propto f^{\alpha}$, with an exponent α of -1.98 (black dashed line), close to the value of $\alpha = -2$ that is expected for free diffusion. (d) 2-dimensional histogram of (x, y) bead position for the red (un-nicked) dataset in a). (e) and (f) show similar data for the black (nicking at 1000 s) and blue (nicked) recordings, respectively. The magnet does not significantly affect the angular position in any of the three traces, as evidenced by the even distribution of positions on the circle. (g) Temporal autocorrelations for the constrained (red) and unconstrained (blue) recordings. Fits to an exponential decay (black solid lines), which describes both diffusion within a harmonic trap and free diffusion are shown in black. The autocorrelation at $\tau = 0$ s is equal to the angular variance, and increases dramatically after the rotational constraint is lost. Similarly, the characteristic timescale increases from $\tau_c = 17.2$ s to 249 s upon loss of rotational constraint. The inset shows a zoom of the autocorrelation for the rotationally constrained trace.
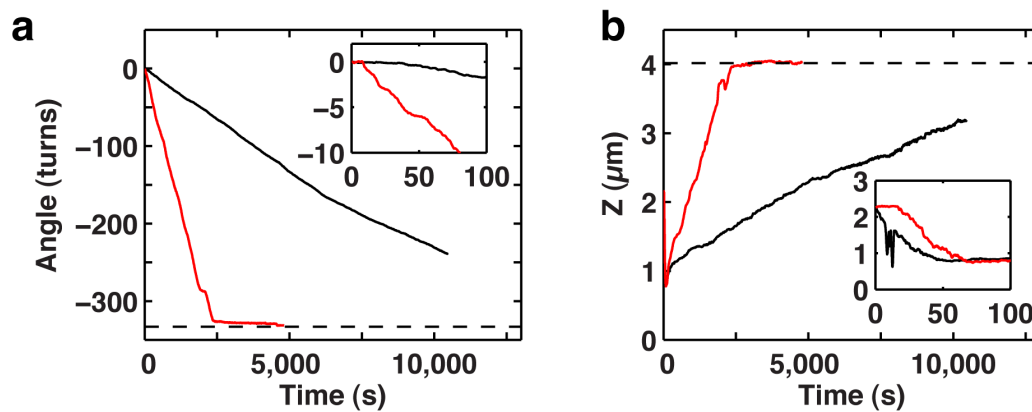
Supplementary Figure S15. The effect of rotational drag on the dynamics of RecA heteroduplex filament assembly on 7.9 kbp DNA under 1.5 pN applied force. (a) The number of rotations θ executed by the bead as a function of time during RecA unwinding of a 7,921 bp DNA molecule tethered to a 1.4 μm radius bead at 1.5 pN pulling force (black trace) and to a 0.5 μm radius bead at 1.5 pN pulling force (red trace, reproduced from Fig. 4). The corresponding unwinding rates are -0.024 turns/s, and -0.14 turns/s, respectively. The inset shows the first 100 s of the traces. (b) Corresponding data for the DNA extension z as a function of time; trace colors as in **a**. The inset shows the first 100 s of the traces (the noise at $\approx$ 15 s in the black trace results from flushing).

Bead	R_{circle} (μm) Tether point in southern hemisphere	R_{circle} (μm) Tether point in northern hemisphere	ϕ (rad)	Predicted Δz (μm)	Measured Δz (μm)
1	0.50	1.58	0.36	3.01	3.52
2	1.53	1.54	1.57^{a}	0.00	-0.02
3	1.22	1.53	1.05	1.43	1.68
4	1.08	1.53	0.88	1.86	2.03
5	0.65	1.57	0.48	2.77	2.76

Supplementary Table S1. The effect of magnet orientation on circle radius and bead height. Results are shown for five independent measurements with 1.4 μm radius beads tethered to 20.6 kbp DNA at a pulling force of 2.5 pN under a carefully aligned cylindrical magnet. [a]In this particular case, we cannot calculate ϕ, since $R_{\mathrm{circle}} > R_{\mathrm{bead}}$ for both magnet orientations. Since flipping the magnet has a negligible effect on both R_{circle} and z, we assume that the bead is tethered at the equator, i.e. $\phi = \pi/2$.

F (pN)	R_bead (μm)	θ_final (turns)	z_final (μm)	Rotation Rate (Hz)	Assembly Rate (RecA/s)	τ_c (s)	γ (pN·nm·ss /rad)
6.5	1.4	-323	4.17	-0.028	0.23	220	76
1.5	1.4			-0.024	0.19	250	89
1.5	0.5	-332	4.02	-0.14	1.12	76	7.3

Supplementary Table S2. RecA unwinding data. Forces are calculated from radial fluctuations as described in the main text. Rotation rates are calculated from linear fits to data shown in Fig. 2 and Supplementary Fig. S15, and converted to RecA assembly rates using our measured twist change of -44.7° per RecA monomer. Tether relaxation timescales are measured prior to RecA addition, by fitting the rotational autocorrelation (Equation 10, Online Methods). Drag coefficients are calculated from the bead radius and circle diameter, as described in Supplementary Methods. The data show that the RecA assembly rate is strongly dependent on the drag coefficient, but only weakly dependent on the applied force.

Method	FOMT	Tethered particle motion	Previous magnet-based measurements	Rotor bead tracking with micropipette and optical trap
References	This work	Yasuda *et al.*, Hayashi & Harada	Harada *et al.*; Han *et al.* ; Arata *et al.*	Bryant *et al.*
Demonstrated capability				
Twist measurement (i.e. rotation angle)	(green)	(green)	(green)	(green)
Force application	(green)	No force application for nucleic acids; fixed force for actin assay (red)	(green)	(green)
Force measurement & calibration	(green)	(red)	(green)	(green)
Length measurement (i.e. z or molecule extension)	(green)	(red)	(red)	(green)
Bias free twist measurement (i.e. trap stiffness $\ll$ DNA stiffness)	(green)	(green)	(red)	(green)
Switch between torque introduction and twist measurement	By changing alignment or introducing a side magnet as in the MTT (green)	(red)	(red)	Due to the presence of a nick, torque introduction requires fluid flow (green)
Demonstrated parameters				
Angular resolution	$\approx$ 0.1° with extra marker; a few degrees without marker	Not specified (likely a few degrees)	$\approx$ 5-10 °	$\approx$ 90°
Force range	0.1 - 10 pN	Not applicable	No precise calibration; $\leq$ 2 pN	15-90 pN
Temporal resolution (τ_c)	$\approx$ 2.5 s with 3.4 kbp DNA	$\approx$ 1.8 s with 0.5 kbp DNA	Not discussed	Not discussed; (with 14.8 kbp DNA and 0.5 μm diameter rotor bead, we estimate $\approx$ 7 s)
Simplicity of the setup				
No requirement for marker bead on main bead	(green)	(red)	(red)	(green)
No requirement for marker internal on the DNA	(green)	(green)	(green)	(red)
No requirement for fluorescence detection	(green)	(green)	(red)	(green)
No requirement for an optical trap	(green)	(green)	(green)	(red)

Method, **continued**	Rotor bead tracking with MT and fluorescence detection	Passive optical torque wrench with microfabricated cylinders	"Soft" electromagnetic tweezers
References	Gore *et al.*	Inman *et al.*	Mosconi *et al.*
Demonstrated capability			
Twist measurement (i.e. rotation angle)	(green)	Not yet demonstrated for tethered particle (red)	(green)
Force application	(green)	(green)	(green)
Force measurement & calibration	(green)	(green)	(green)
Length measurement (i.e. z or molecule extension)	(green)	(green)	(green)
Bias free twist measurement (i.e. trap stiffness $\ll$ DNA stiffness)	(green)	(red)	(red)
Switch between torque introduction and twist measurement	Due to the presence of a nick, torque introduction requires fluid flow (green)	Not demonstrated for tethered particle (red)	(green)
Demonstrated parameters			
Angular resolution	$\approx 3°$	Not specified (likely $\geq$ 10° judging from Fig. 1c of Inman *et al.*)	Not specified (likely $\leq$ 0.5° judging from Fig. 5a of Mosconi *et al.*)
Force range	0.35-18 pN	Not specified ($\geq$ 1 pN judging from Forth *et al.*)	0.05-2 pN
Temporal resolution (τ_c)	$\approx$ 0.5 s with 1.1 kbp DNA	Not applicable; no tether yet	$\sim$100-1000 s, due to the large beads in the current implementation
Simplicity of the setup			
No requirement for marker bead on main bead	(green)	(green)	(red)
No requirement for marker internal on the DNA	(red)	(green)	(green)
No requirement for fluorescence detection	(red)	(green)	(green)
No requirement for an optical trap	(green)	(red)	(green)

Supplementary Table S3. Comparison of rotational tracking methods. The comparison of alternative approaches for directly tracking the rotation of nucleic acid tethers was compiled based on the results presented in this work for the FOMT and based on published work for the other methods (see references in the second row). The table employs green and red color-coding, whereby green coloring reflects a positive assessment whereas red coloring reflects a negative assessment of the points or characteristics listed in the first column. References refer to the bibliography in the main text.

Supplementary references

[38] Lipfert, J., Klijnhout, S. & Dekker, N. H. Torsional sensing of small-molecule binding using magnetic tweezers. *Nucleic Acids Res.* **38**, 7122–7132 (2010).

[39] Fonnum, G., Johansson, C., Molteberg, A., Morup, S. & Aksnes, E. Characterization of dynabeads by magnetization measurements and mössbauer spectroscopy. *J. Magn. Magn. Mat.* **293**, 41–47 (2005).

[40] Neuman, K. C., Lionnet, T. & Allemand, J.-F. Single-molecule micromanipulation techniques. *Annu. Rev. Mater. Res.* **37**, 33–67 (2007).